

# Wood-Derived, Monolithic Chainmail Electrocatalyst for Biomass-Assisted Hydrogen Production

Di Li, Zengyong Li, Zhongxin Chen, Ge Shi, Lu Wang, Zehong Chen, Wenguang Tu, Ruidong Xia, Emmanuel I. Iwuoha, Chuanfu Liu,\* and Xinwen Peng\*

The chainmail catalyst by encapsulating an active species within the carbon support is a well-established concept to endorse extraordinary stability for catalytic reactions under harsh conditions. Conventional chainmail catalysts inevitably suffer from poor accessibility to active sites, leading to extra voltage to compensate the sluggish diffusion kinetics in electrocatalysis. Herein, the naturally abundant wood material is converted into a monolithic chainmail electrocatalyst by encapsulating cobalt nanoparticles within N-doped carbonized wood. Such a monolithic chainmail catalyst is employed directly as electrode for hydrogen evolution (HER), oxygen evolution (OER), and monosaccharide oxidation reactions (MOR) with benchmark performance. By coupling the HER with MOR, the electrolyzer equipped with the monolithic chainmail catalyst allows hydrogen production at a current density of 100 mA cm<sup>-2</sup> with a full cell voltage of only 1.36 V. Such design of wood-derived chainmail catalyst provides a promising way to fabricate robust electrocatalysts for future production of hydrogen and value-added chemicals.

phosphides,<sup>[11–14]</sup> nitrides,<sup>[15,16]</sup> sulfides,<sup>[17–19]</sup> and carbides<sup>[20–22]</sup> have been recently developed to replace expensive platinum (Pt/C)- and ruthenium and iridium dioxide (Ru/IrO<sub>2</sub>) based catalysts. Nevertheless, the degradation of catalytic activity and stability of these catalysts occurs by corrosion, oxidation, and dissolution of active species under harsh conditions such as highly acidic or alkaline media, high overpotentials in electrocatalysis.<sup>[23,24]</sup>

To this end, a concept of “chainmail catalyst” has been developed by Bao et al. to endorse extraordinary catalyst stability by encapsulating the metal active species within the carbon support.<sup>[25–27]</sup> In these chainmail catalysts, the stable graphitic shell not only effectively protects the internal active species from the corrosive environment but also


provides a high-speed channel to allow the rapid electron transfer toward the active species, leading to the enhanced catalytic capability.<sup>[28,29]</sup> Despite proven as effective, conventional chainmail electrocatalysts in powder form usually involve tedious slurry-based electrode preparation process, which inevitably masks the catalytic metal active sites and also limits electron transfer and mass diffusion.<sup>[30,31]</sup> Moreover, because of the weak interaction between the chainmail electrocatalyst and conductive substrate, the electrocatalyst could peel off from the conductive substrate during the catalytic reaction process, resulting in a decrease in the stability of catalyst.<sup>[32]</sup> Therefore, it is crucial for the rational design of sustainable, binder-free, and self-supporting chainmail electrocatalyst to maximize the exposure of the active

## 1. Introduction

Electricity-driven water splitting to produce energy-dense hydrogen is a promising strategy for natural water-to-chemical fuel conversion.<sup>[1–3]</sup> However, the energy efficiency and practical application of water splitting is greatly impeded by the sluggish kinetic electrochemical reactions, including hydrogen evolution reaction (HER) and oxygen evolution reaction (OER).<sup>[4–7]</sup> Up to now, noble metal-based catalysts, such as Pt-based or Ru/IrO<sub>2</sub>-based compounds, are considered as the benchmark electrocatalysts for above electrochemical reactions. Unfortunately, they suffer from high cost and scarcity.<sup>[8–10]</sup> In terms of availability, a series of efficient electrocatalysts including transition metal

D. Li, Z. Li, G. Shi, Z. Chen, C. Liu, X. Peng  
State Key Laboratory of Pulp and Paper Engineering  
School of Light Industry and Engineering  
South China University of Technology  
381 Wushan Road, Guangzhou 510641, China  
E-mail: chfliu@scut.edu.cn; fexwpeng@scut.edu.cn

Z. Chen, L. Wang, W. Tu  
School of Science and Engineering  
The Chinese University of Hong Kong  
Shenzhen 518172, China

 The ORCID identification number(s) for the author(s) of this article can be found under <https://doi.org/10.1002/aenm.202300427>

DOI: 10.1002/aenm.202300427

G. Shi  
Centre for Catalysis and Clean Energy  
Griffith University  
Gold Coast, Queensland 4222, Australia

R. Xia  
School of Communications and Information Engineering  
Nanjing University of Posts and Telecommunications  
Nanjing 210003, China

E. I. Iwuoha  
SensorLab  
Department of Chemistry  
University of the Western Cape  
Bellville, Cape Town 7535, South Africa

sites and enable faster mass diffusion. In addition, the main obstacle to current water electrolysis technology is that up to 90% of the electricity is consumed by oxygen evolution (OER), resulting in expensive hydrogen production.<sup>[33]</sup> This thermodynamic constraint indicates that it is difficult for HER-OER coupling to significantly reduce power consumption. Recently, utilizing electrochemical oxidation of organic molecules that are thermodynamically favorable to replace the sluggish kinetic OER can not only avoid the production of O<sub>2</sub> and reduce the voltage but also provide a higher current density under the condition of low input voltage, thus improving the energy conversion efficiency.<sup>[34–37]</sup> Undoubtedly, monosaccharides derived from lignocellulose, the most abundant form of biomass, are definitely promising due to overcoming the resource scalability mismatch and reducing energy costs.<sup>[38,39]</sup> Encouragingly, carbon frame materials derived from natural wood have inherent three-dimensional layered porous structure, high electrical conductivity, excellent corrosion resistance and low cost, and are considered as promising candidate substrate materials for the preparation of high-performance electrodes.<sup>[40]</sup> For instance, Hu et al. prepared few-graphene-layer-encapsulated nickel iron alloy (N-C-NiFe) nanoparticles in the porous carbonized wood via the ultrafast Joule heating as highly effective electrocatalyst for HER in acid solution.<sup>[41]</sup> Hui and co-workers also demonstrated that NiP/Poplar wood can be employed as efficient HER electrocatalyst.<sup>[42]</sup> Moreover, Chen et al. developed a MOF-derived CoNi bimetallic nanoparticles into carbonized wood framework (CoNiNP-N@CoNi/CW), yielding remarkable catalytic performances toward HER.<sup>[43]</sup> Nevertheless, the active metals tend to agglomerate and distribute unevenly in the constructed three-dimensional substrate, which leads to the obstruction of electron transfer and electrolyte diffusion, thus limiting their catalytic performance. It is still a big challenge to realize the efficient expression of HER, OER, and MOR functions on an integrated electrode. Therefore, the development of a practical and facile strategy for the synthesis of highly efficient trifunctional wood-based electrodes is particularly urgent for coupled biomass oxidation and water splitting in pairs to generate hydrogen and high value-added chemicals.

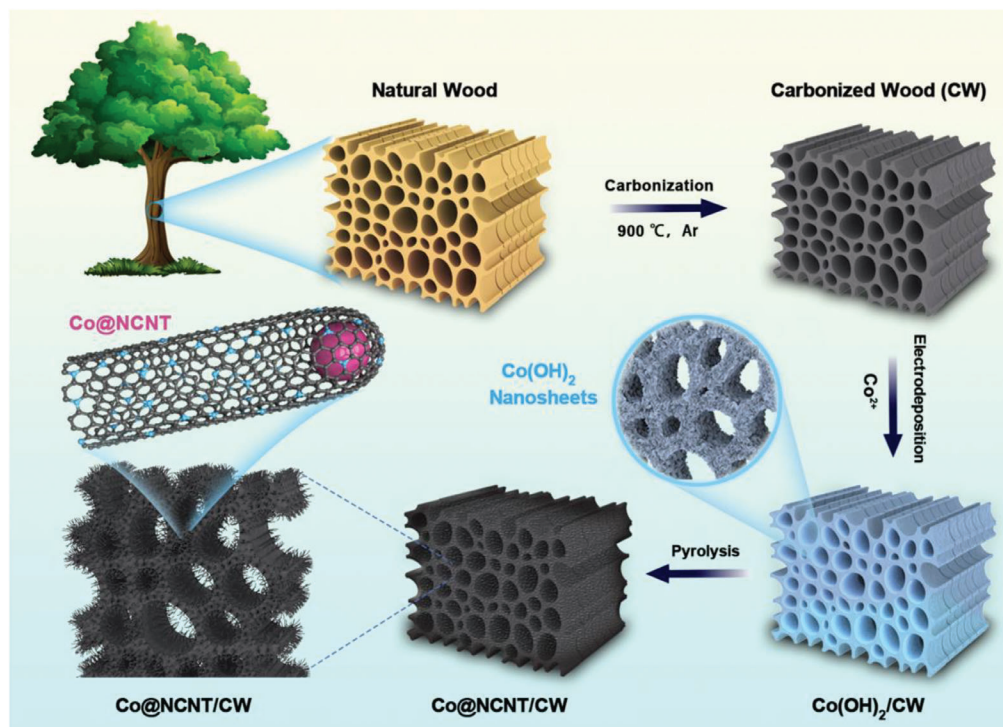
Herein, a monolithic wood-based hierarchically porous chainmail electrocatalyst is produced by encapsulating the cobalt nanoparticles within the N-doped carbon nanotube in situ grown on carbonized wood (Co@NCNT/CW). The open, well-arranged 3D directional microchannels of Co@NCNT/CW can facilitate the electrolyte transport in electrodes and ensure rapid gas diffusion. The monolithic chainmail electrocatalyst exhibits impressive trifunctional electrocatalytic performance toward hydrogen evolution reaction (HER), oxygen evolution reaction (OER), and monosaccharide oxidation reaction (MOR). The Co@NCNT/CW displays a low overpotential of 263 mV to reach the high current density of 500 mA cm<sup>-2</sup> for 100 h operation in HER. Notably, in a two-electrode hybrid electrolyzer utilizing the Co@NCNT/CW as both cathode and anode for coupled HER and MOR, a lower cell voltage of only 1.36 V is required to generate a current density of 100 mA cm<sup>-2</sup>, which is 420 mV lower than that required for traditional overall water splitting. Meanwhile, the hydrogen and value-added chemicals can be obtained at the cathode and the anode, synchronously and respectively.

## 2. Results and Discussion

The synthetic route of Co@NCNT/CW is illustrated in **Scheme 1**. Carbonized wood (CW) was prepared by direct pyrolysis of natural beech wood at 900 °C. Scanning electron microscopy (SEM) images show the preservation of hierarchically porous structure with highly orientated open channels in CW after pyrolysis (Figures S1 and S2, Supporting Information). The cobalt hydroxide (Co(OH)<sub>2</sub>) nanosheets are in situ electrochemically grown on the surface of these channels inside the CW bulk to produce the bulk Co(OH)<sub>2</sub>/CW (Figure S3, Supporting Information). Then, the Co(OH)<sub>2</sub>/CW acts as cobalt precursor for subsequent reaction with melamine to form the encapsulated Co nanoparticles within the N-doped carbon nanotubes on carbonized wood (Co@NCNT/CW) (**Figure 1a**). Such monolithic chainmail catalyst retains extraordinary mechanical strength from natural wood, which can withstand >1300 times of its own weight without obvious structure damage (Figure S4, Supporting Information).

As shown in Figure 1b,c, the SEM images of Co@NCNT/CW confirm full coverage of Co@NCNTs on each vertical channel of CW. The inset in Figure 1c displays the interlaced nanotubes with the diameter of ≈50 nm. Compared with the original wood, the orientated microchannels are well-retained in the parallel, as indicated in Figure 1d. Obviously, the interlaced Co@NCNTs are grown uniformly in the pores of the CW, forming a monolithic hierarchical structure (Figure 1e,f). Benefiting from the low-tortuosity and hierarchically porous structure, the electrolyte can penetrate into pores of the Co@NCNT/CW, and the gas generated on the catalyst surface is favorable to release from the hierarchically porous with ensure the pathway of mass transfer.

Additionally, the uniformly integration of nanotubes on the pores inside the CW can provide electron “highways,” which allow for rapid charge transfer during the catalytic reaction. Furthermore, the high-resolution transmission electron microscopy (HRTEM) images in Figure 1g–i reveal the encapsulation of Co nanoparticles in N-doped carbon nanotubes with a typical bamboo-like structure. After carbonization with melamine, N-doped highly crystalline graphite carbon is formed as the coating layer. The lattice fringe spacing of 0.34 nm is assigned to the (002) plane of graphite carbon, while two other lattice fringes of 0.20 and 0.18 nm can be indexed to (111) and (200) facets of metallic Co nanoparticles (30–50 nm in diameter). The selected area electron diffraction (SAED) pattern (inset in Figure 1i) confirms the polycrystalline structure of metallic Co. Moreover, the energy dispersive spectrometer (EDS) mapping images in Figure 1j demonstrate the uniform distribution of C, N, O, and Co elements in the entire pores and surface of CW. The relative contents of N and Co are determined as 4.36 and 6.23 wt% from elemental analysis and inductively coupled plasma (ICP), respectively. To investigate the effect of melamine during carbonization, a series of samples with different amount of melamine were prepared. Direct carbonization without melamine will lead to agglomeration and formation of random clusters of Co (Figure S5, Supporting Information). With the addition of 0.5 g of melamine, short nanotubes with larger diameters are formed within the pores of CW (Figure S6a–c, Supporting Information). With more melamine, the length and density of nanotubes increase gradually (Figure S6d–f, Supporting Information), and finally leads to



**Scheme 1.** Schematic of the wood-derived, monolithic chainmail catalyst.

overgrown nanotubes (2 g melamine) that blocking the mass diffusion within vertical channels of CW (Figure S6g–i, Supporting Information).

Chemical composition of the chainmail catalyst was verified by X-ray diffraction (XRD) and X-ray photoelectron spectroscopy (XPS). Phase composition was determined by XRD. As shown in **Figure 2a**, the characteristic peaks located at 44.2, 51.5, and 75.9° are well-indexed to the (111), (200), and (220) planes of metallic Co in the Co@NCNT/CW, respectively (PDF#15-0806).<sup>[44]</sup> The peaks at 24.8 and 43.6° are assignable to the (002) and (101) facets of graphite carbon.<sup>[45]</sup> XPS spectra and the corresponding surface elements content of Co@NCNT/CW are shown in **Figure 2b–d** and Table S1 (Supporting Information). The high-resolution C 1s spectrum can be fitted into three peaks located at 284.7, 285.9, and 290.3 eV corresponding to the C=C/C–C, C–N, and C=O species, respectively.<sup>[13]</sup> The high-resolution N 1s spectrum displays five types of N species, namely, the pyridinic-N (398.4 eV), Co–N<sub>x</sub> (399.2 eV), pyrrolic-N (400.1 eV), graphitic-N (401.2 eV), and oxidized-N (402.8 eV).<sup>[46]</sup> Generally, the introduction of N atom into carbon material can adjust the electronic structure of adjacent C atom, resulting in the redistribution of charge, and thus stimulating the catalytic activity of C site.<sup>[47]</sup> In addition, N-doped carbon layer can establish significant synergies with active metals at the interface compared with undoped N catalysts, thus greatly improving the electrocatalytic performances.<sup>[48]</sup> In the high-resolution Co 2p spectrum, the Co 2p<sub>3/2</sub> can be deconvoluted into three peaks located at 778.8, 779.6, and 781.3 eV, corresponding to the Co<sup>0</sup>, Co–N<sub>x</sub>, and Co<sup>2+</sup>, respectively.<sup>[49]</sup> The presence of Co<sup>2+</sup> is attributed to the surface oxidation of cobalt nanoparticles,<sup>[11]</sup> while the Co–N<sub>x</sub> species

can improve the catalytic activity for HER and OER.<sup>[50,51]</sup> Detailed verification of chemical compositions with various melamine loadings are provided in **Figure S7** (Supporting Information).

Moreover, Co@NCNT/CW possesses a higher Brunauer–Emmett–Teller (BET) surface area of 741 m<sup>2</sup> g<sup>−1</sup> compared with Co(OH)<sub>2</sub>/CW (595 m<sup>2</sup> g<sup>−1</sup>) and CW (440 m<sup>2</sup> g<sup>−1</sup>) (**Figure 2e**) owing to its hierarchically porous structure. The corresponding pore size distributions of samples (**Figure S8**, Supporting Information) reveal the dominance of micropores and mesopores, which allows fast transport kinetics of reactants to active sites. Typical defective (D band) and graphitic (G band) signals located at 1355 and 1582 cm<sup>−1</sup> are observed in the Raman spectra. The corresponding strength ratio (*I<sub>D</sub>*/*I<sub>G</sub>*) reveals the defect density and graphitization degree in carbon materials. Co@NCNT/CW shows a larger intensity ratio (*I<sub>D</sub>*/*I<sub>G</sub>*) of 1.06 compared with control samples. This finding suggests a slightly higher amount of defect formation in Co@NCNT/CW during carbonization, which can be beneficial for enhancing electrocatalytic activity. Such monolithic catalyst also possesses excellent hydrophilicity with a water contact angle of 9.7°, which ensures the immerse contact between the electrolyte and catalyst for fast ion transport (**Figure S9**, Supporting Information).

Electrochemical performance of monolithic Co@NCNT/CW electrode was evaluated in a standard three-electrode system in 1 mKOH. Linear sweep voltammetry (LSV) in **Figure 3a** confirms an excellent HER activity for large current density operation for Co@NCNT/CW. The overpotential for Co@NCNT/CW to reach 50 mA cm<sup>−2</sup> (155 mV) is significantly lower than those of Co(OH)<sub>2</sub>/CW (295 mV) and Co/CW (431 mV) (**Figure 3b**).



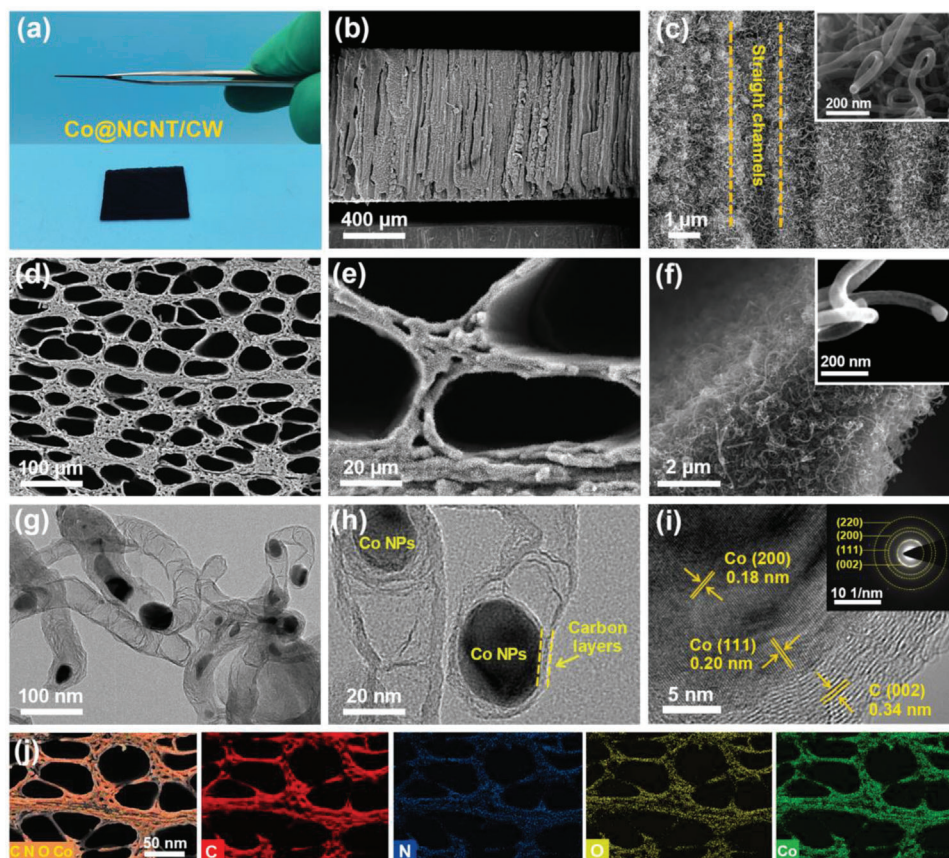


**Figure 1.** Hierarchically porous structure of monolithic electrode. a) Photo of the monolithic Co@NCNT/CW sample. b,c) SEM images of Co@NCNT/CW in the vertical and d–f) parallel direction. g–i) TEM and HRTEM images of the Co@NCNT/CW. Inset of (i) shows typical SAED pattern. j) The corresponding EDS mappings.

Notably, the overpotentials for Co@NCNT/CW to achieve large current densities of 200 and 500 mA cm<sup>-2</sup> are only 238 and 263 mV, respectively, which are superior to those of commercial Pt/C catalyst. The Tafel slope of Co@NCNT/CW shows a smaller value of 53 mV dec<sup>-1</sup> compared with control samples, revealing the faster kinetic reaction of Co@NCNT/CW (Figure S10, Supporting Information). In order to further investigate the intrinsic catalytic activity of Co@NCNT/CW, the electrochemical active area (ECSA) and electrochemical impedance spectroscopy (EIS) of the catalysts were tested (Figures S11 and S12, Supporting Information). The Co@NCNT/CW exhibits a high double layer capacitance ( $C_{dl}$ ) value of 82.9 mF cm<sup>-2</sup>, which is significantly higher than that of Co(OH)<sub>2</sub>/CW (64.4 mF cm<sup>-2</sup>) and Co/CW (47.9 mF cm<sup>-2</sup>). The results suggest that Co@NCNT/CW catalyst can endow more catalytic active sites in the electrocatalytic process. In addition, the charge transfer resistance ( $R_{ct}$ ) of Co@NCNT/CW catalyst was only 3.4 Ω, much lower than that of Co(OH)<sub>2</sub>/CW and Co/CW, revealing the faster electron transfer rate of Co@NCNT/CW during the catalytic process. The lower charge transfer resistance of Co@NCNT/CW can be attributed to the fact that the integrated structure formed by CW and Co@NCNTs makes it more conductive and promotes rapid electron transfer. Owing to its hierarchically porous structure and unique chainmail coating, our Co@NCNT/CW

outperforms the reported non-noble metal catalyst in the performance comparison for HER (Figure 3c and Table S2, Supporting Information). No catalyst degradation could be observed in the accelerated cycling test for 3000 cycles (Figure S13, Supporting Information), the 100-h chronoamperometric test (Figure 3d) and postanalysis on the structural integrity (Figures S14 and S15, Supporting Information). We also conducted similar experiments to verify the catalytic activity of Co@NCNT/CW for OER. As shown in Figure 3e,f, the Co@NCNT/CW electrode affords the best OER activity among all the samples including IrO<sub>2</sub>, with a lower overpotential of 0.37 V at 100 mA cm<sup>-2</sup>. Moreover, such monolithic catalyst possesses outstanding durability in the accelerated cycling test for 3000 cycles and chronoamperometric test for 24 h at large current density without significant attenuation (the inset of Figure 3f). Similarly, the Co@NCNT/CW electrode shows the well-maintained carbon nanotubes structure after the OER test except that the surface becomes a little rougher compared with the initial state (Figure S16, Supporting Information). This change can be attributed to the surface reconfiguration of the catalyst during the OER process. The HRTEM images also show that the Co nanoparticle was well encapsulated into carbon nanotubes without significant structural damage (Figure S17, Supporting Information). In addition, the high-resolution scans of Co 2p and O 1s spectra show new cobalt-oxide peaks,

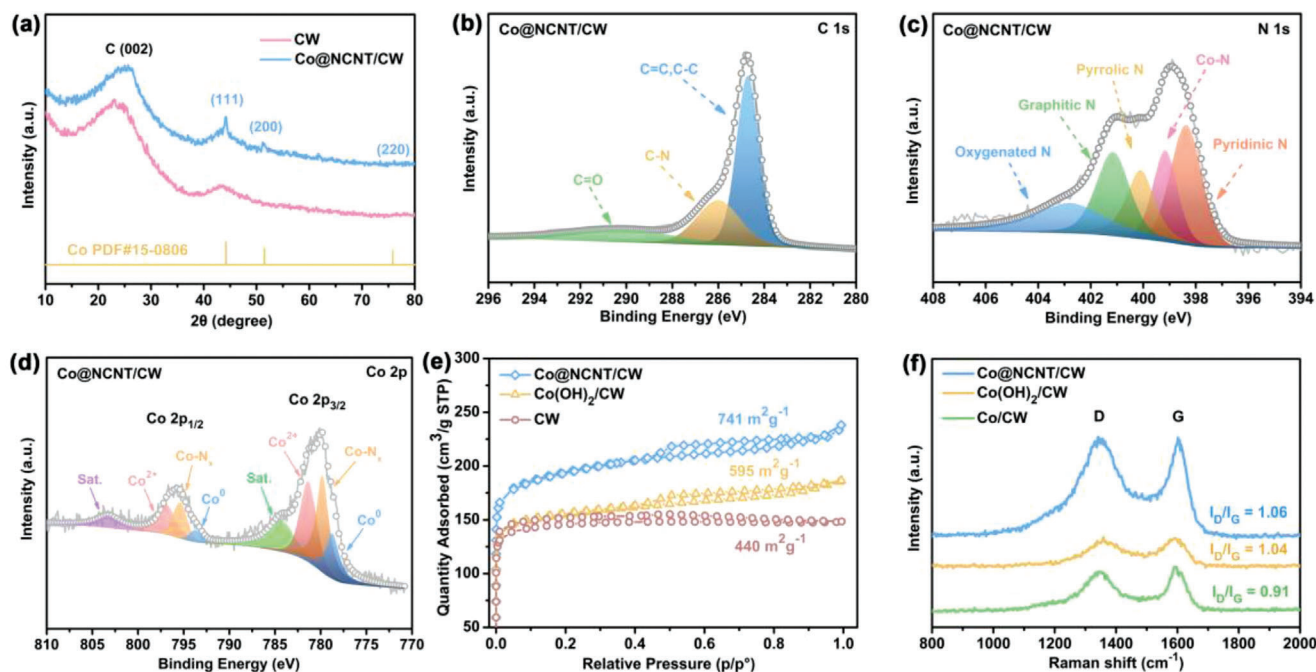


**Figure 2.** Chemical composition of the chainmail catalyst. a) XRD spectra. b) High-resolution XPS spectra of C 1s, c) N 1s, and d) Co 2p for Co@NCNT/CW. e)  $N_2$  adsorption–desorption isotherms of Co@NCNT/CW, Co(OH)<sub>2</sub>/CW and CW. f) Raman spectra of Co@NCNT/CW, Co(OH)<sub>2</sub>/CW, and Co/CW.

further confirming the in situ electrochemical oxidation on the surface of Co@NCNT/CW catalyst to form cobalt oxides or hydroxides, which is considered to be the actual catalytic active site in the OER catalytic process (Figure S18, Supporting Information). For overall water splitting, a two-electrode electrolyzer was constructed by directly using monolithic Co@NCNT/CW as both the cathode and anode electrocatalysts (Figure 3g). The Co@NCNT/CW || Co@NCNT/CW electrode exhibits excellent activity for water splitting with nearly 100% Faradaic efficiency (Figure 3h and Figure S19, Supporting Information). Notably, the Co@NCNT/CW || Co@NCNT/CW electrode possesses an extraordinary durability for a continuous 100 operational hours at 100 mA cm<sup>-2</sup> for water splitting, which is superior to most lately reported non-noble metal electrocatalysts (Figure 3i and Table S3, Supporting Information). The remarkable stability of Co@NCNT/CW could be attributed to its unique monolithic 3D structure and chainmail coating. In addition, conventional electrochemical devices for gas-involving reactions usually adopt a gas diffusion electrode (GDE) configuration to modulate the gas/liquid interface and maximize the mass transport kinetics. Compared with powder-based chainmail catalyst, our monolithic Co@NCNT/CW electrode allows direct usage as GDE for devices, thus avoiding the use of nonactive components in electrode fabrication (Figure S20, Supporting Information). Such chainmail catalyst exhibits high electrocatalytic activity when directly used as a GDE. In addition, the MEA electrolyzer also shows no significant performance degradation during 25 h of continuous water splitting, which further confirms its feasibility for MEA water splitting.

A major challenge in water splitting devices lies in the sluggish kinetics of OER, which consumes significant amount of elec-

tricity and produces oxygen with little value.<sup>[52]</sup> The coupling of biomass oxidation with hydrogen evolution is a better alternative to conventional water-splitting devices for hydrogen production at a reduced cost.<sup>[53,54]</sup> Thus, monosaccharide oxidation reaction (MOR) was selected for such hybrid electrolyzer. The catalytic performance of Co@NCNT/CW toward MOR at anode was examined in 1 M KOH. As shown in Figure 4a, the addition of 0.1 M xylose results in a significant reduction in overpotential to achieve the current density of 50 mA cm<sup>-2</sup> (1.13 vs 1.54 V) owing to much favorable kinetics of MOR than OER (Figure 4b,c). Such MOR activity is positively correlated to the concentration of xylose (Figure S21, Supporting Information).

Owing to its trifunctional activity toward HER, OER, and MOR, a hybrid electrolyzer was assembled only composed of monolithic Co@NCNT/CW as cathode and anode (Figure 4d). By switching from pure overall water splitting to hybrid water electrolysis, the Co@NCNT/CW || Co@NCNT/CW electrolyzer allows hydrogen production at 100 mA cm<sup>-2</sup> with a cell voltage of 1.36 V, which is 420 mV lower than that of pure water-splitting device (Figure 4e,f). This is superior to most other reported configurations, including standard Pt/C || IrO<sub>2</sub> electrolyzer (Table S4, Supporting Information). Moreover, the chronoamperometry test in five consecutive runs for hybrid water electrolysis (Figure 4g and Figure S22, Supporting Information) reveals a gradually decreased current density due to consumption of xylose, where the performance can be recovered by supplying fresh electrolyte. The Faradaic efficiency for cathodic H<sub>2</sub> production reaches 97.6% and is maintained even after five cycles (Figure 4h,i). Such concept can be further extended to the oxidation of other monosaccharide (glucose, arabinose, and fructose in Figure S23, Supporting Information), implying the conceptual



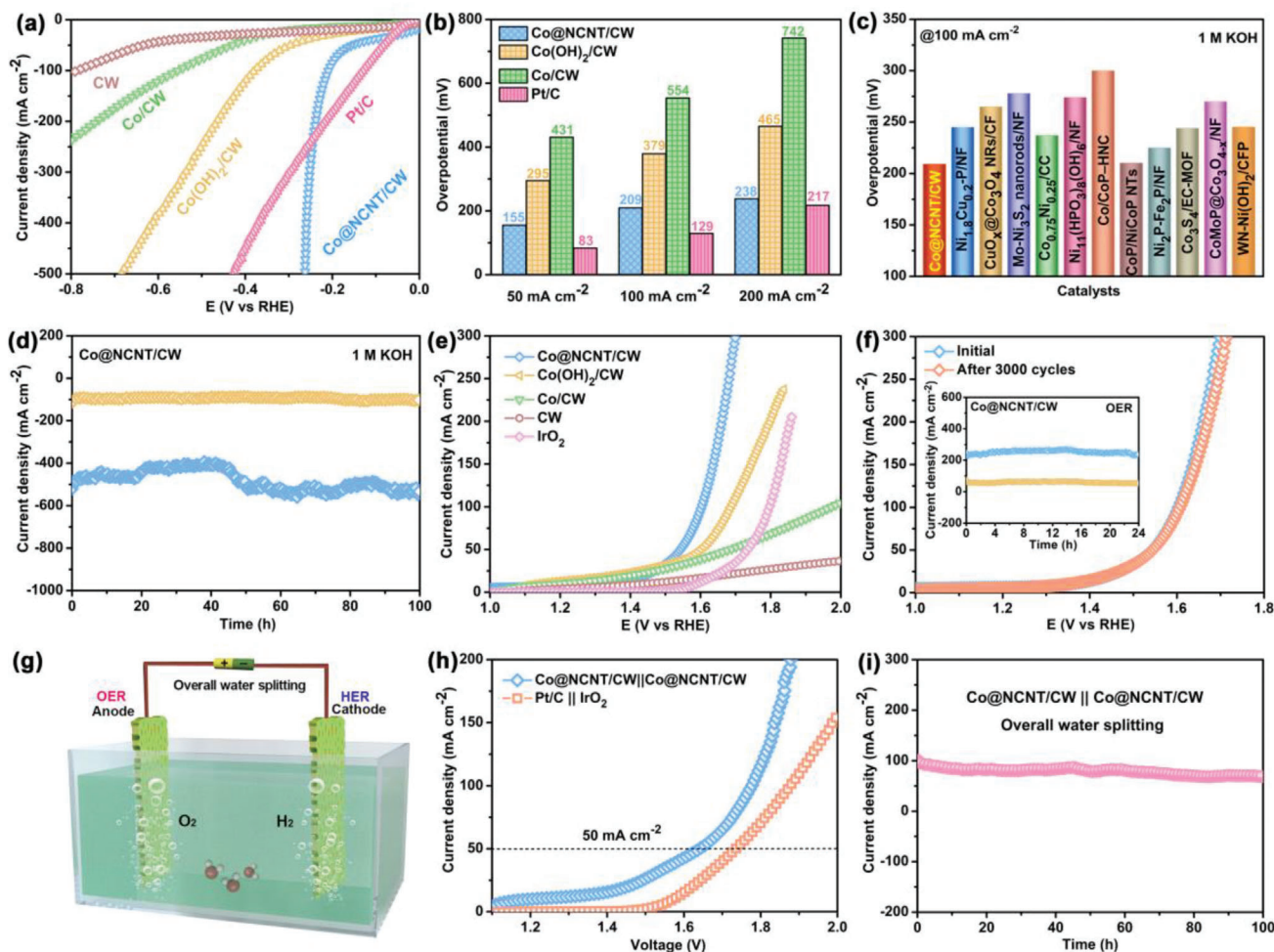


**Figure 3.** Electrochemical performance in water splitting. a) Polarization curves for HER activity and b) corresponding overpotentials at different current densities of Co@NCNT/CW, Co(OH)<sub>2</sub>/CW, Co/CW, CW, and Pt/C for HER in 1 M KOH. c) Comparison in the overpotentials at 100 mA cm<sup>-2</sup> for the Co@NCNT/CW and other transition metal catalysts. d) An 100-h chronoamperometric test at large current density of 500 mA cm<sup>-2</sup> for HER in 1 M KOH. e) Polarization curves for OER activity. f) Accelerated cycling test (3000 cycles) for the Co@NCNT/CW in 1 M KOH solution. Inset shows the 24-h chronoamperometric test. g) Schematic diagram of an electrolyzer for water splitting. h) Polarization curves of the Co@NCNT/CW || Co@NCNT/CW two-electrode electrolyzer in 1 M KOH for water splitting. i) Chronopotentiometric curves of water electrolysis for 100 h at 100 mA cm<sup>-2</sup> in 1 M KOH.

advantage in the energy-saving hydrogen production and paired generation of valuable chemicals.

Oxidation products at the anode were monitored by high-performance liquid chromatography (HPLC) in Figures S24–S26 (Supporting Information). After continuous operation of 15 h, more than 97.3% of xylose has been converted into oxidized products, including lactic acid (29.4% selectivity), formic acid (34.0%), and other undetectable products. A plausible mechanism is proposed in Figure S27 (Supporting Information) for the reaction pathway of xylose oxidation to organic acids based on previous reports and experimental results.<sup>[55,56]</sup> In general, the  $\alpha$ -oxidation or  $\beta$ -oxidation of xylose occurs to form the intermediates and formic acid. Isomerization of xylose also happens, leading to the oxidation into glyceraldehyde and oxalic acid via the Retro-aldol reaction and formation of lactic acid as final product. Further analysis of surface composition by XPS implies the formation of high-valent cobalt species during MOR, resulting in the disappearance

of metallic Co peaks at 778.8 and 793.6 eV, and the formation of cobalt hydroxide or hydroxyl oxide at 780.2 eV (Figure S28, Supporting Information). This is supported by new peaks for the Co–O bonds at 529.8 eV in the O 1s spectrum (Figure S28b, Supporting Information).

Density functional theory (DFT) calculation was performed to reveal the interaction between Co nanoparticles and N-doped carbon nanotubes during MOR and HER. Initial step of water splitting in alkaline medium involves the adsorption of H<sub>2</sub>O molecule on the catalyst surface, which is also the kinetic-limiting step. Optimization of the chainmail catalyst was constructed for H<sub>2</sub>O and xylose adsorption on the C and N sites of Co@NCNT in Figure 5a and Figure S29 (Supporting Information). As shown in Figure 5b, water molecule is preferably adsorbed on the C site than the N site from adsorption energy calculation (–0.146 vs –0.068 eV in  $\Delta G_{\text{H}_2\text{O}}$ ). This is attributed to the electron donation from the lone pair of nearby nitrogen atoms according to

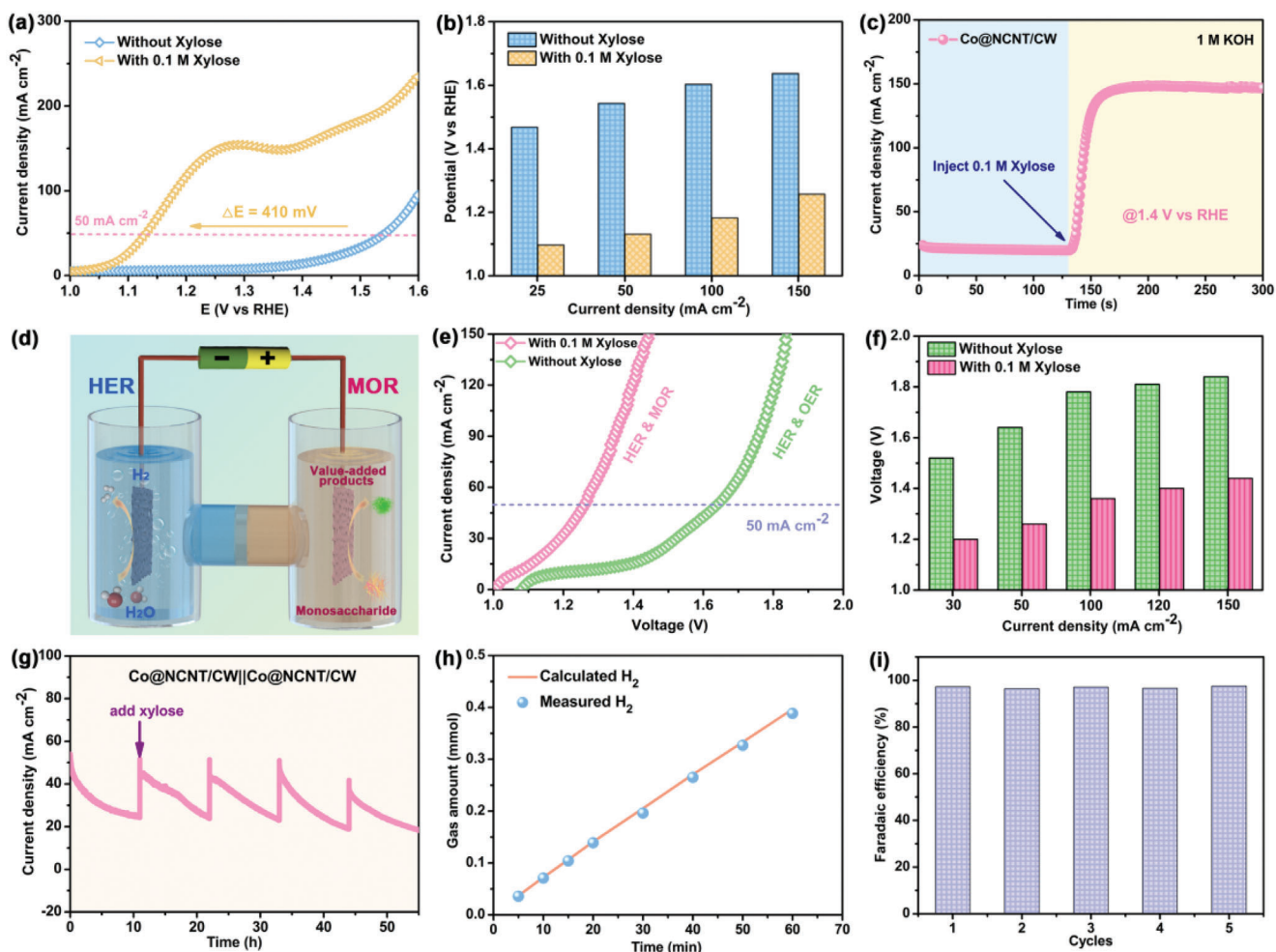


**Figure 4.** Hybrid electrolyzer for hydrogen production. a) Polarization curves of Co@NCNT/CW with and without 0.1 M xylose in 1 M KOH. b) Comparison in anodic potentials at different current densities. c) Chronoamperometry curve of Co@NCNT/CW in 1 M KOH. d) Schematic illustration of a hybrid electrolyzer with trifunctional Co@NCNT/CW for HER, OER, and MOR. e) Polarization curves of Co@NCNT/CW || Co@NCNT/CW in 1 M KOH with and without 0.1 M xylose. f) Comparison in the corresponding cell voltage to reach desired current densities. g) Chronoamperometry curve with the intermittent addition of 0.05 M xylose. h) Comparison in the actual and theoretical  $H_2$  production rate. i) Faradaic efficiency of the Co@NCNT/CW for  $H_2$  production under five consecutive cycles.

previous reports.<sup>[57,58]</sup> The adsorption of xylose on Co@NCNT ( $-0.328$  eV) is much stronger than water, leading to preferable oxidation of xylose rather than oxygen evolution at the same voltage (Figure 5c).

Further calculation on the reactive pathway of  $H_2O$  dissociation reveals that the N-doping level has a profound impact on the catalytic activity. As shown in Figure 5d and Figure S30 (Supporting Information), the energy barrier for water dissociation on the Co@NCNT-12% surface is only 0.618 eV compared with 3.338 and 2.304 eV for Co@NCNT-0% and 4%. It also has a more thermodynamically neutral free energy of hydrogen adsorption ( $\Delta G_{H^*}$ ) value of 0.476 eV, promoting proton adsorption and desorption owing to strong synergistic effect in the chainmail catalyst (Figure S31, Supporting Information). This is supported by the density of electronic states (DOS) calculations of Co and Co@NCNT in Figure 5e. The electron state density at the Fermi level of Co@NCNT is higher than that of Co, indicating an enhanced intrinsic conductivity and synergistic effect. Above DFT

calculations reveal that the presence of N-doped carbon nanotube can optimize the catalytic electronic configuration of Co nanoparticles to synergistically improve the catalytic activity. The superiority of monolithic Co@NCNT/CW as a trifunctional chainmail electrocatalyst is proved theoretically, also confirming its potential for practical application.

### 3. Conclusions

In summary, we have developed a wood-derived, monolithic chainmail catalyst (Co@NCNT/CW) as trifunctional gas diffusional electrode in a hybrid electrolyzer to produce hydrogen and value-added chemicals. Taking advantages of its hierarchically porous structure and metal-substrate synergistic effect, our chainmail catalyst outperforms other transition metal catalysts for water electrolysis during long-term (100 h) and large current density operations. By coupling the HER with MOR, the full cell voltage to reach  $100 \text{ mA cm}^{-2}$  dramatically reduces to 1.36 V for

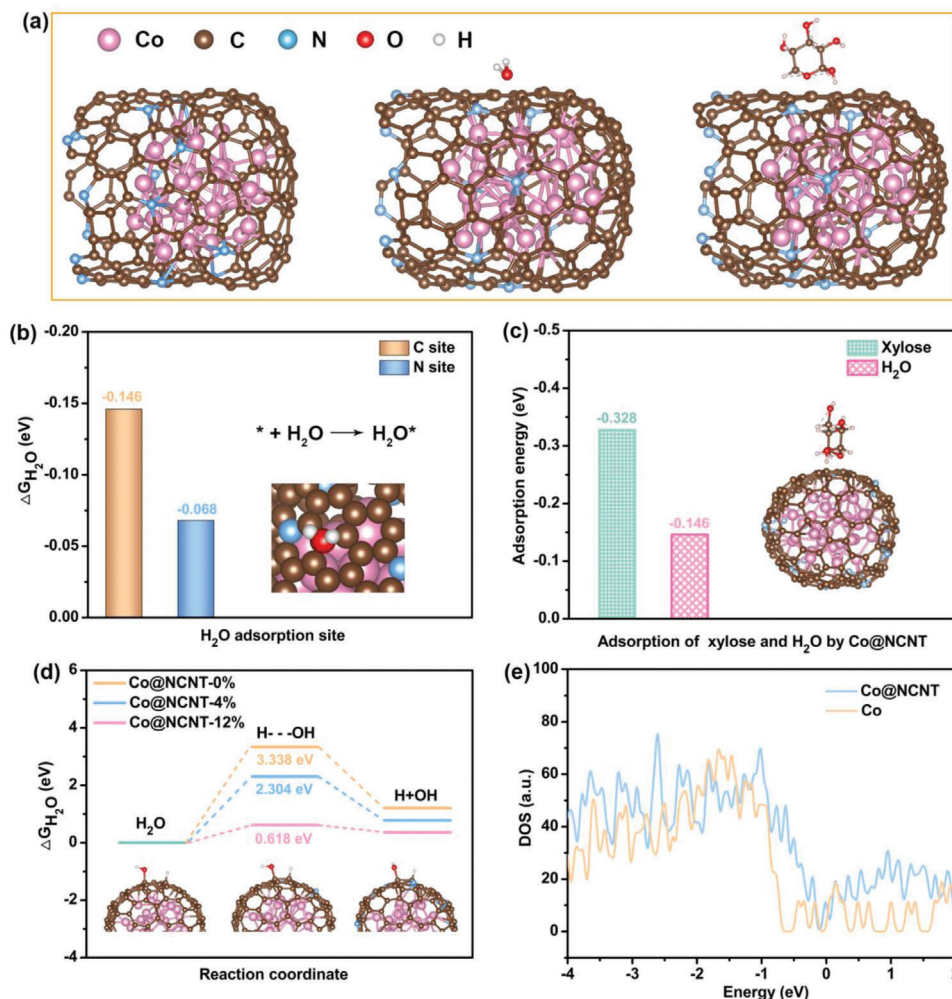


**Figure 5.** DFT calculated reaction mechanism. a) Optimized DFT models and b,c) calculated adsorption energy of H<sub>2</sub>O and xylose molecules on the surface of Co@NCNT. d) The calculated reaction free energy of the H<sub>2</sub>O dissociation on the Co@NCNT surface at various nitrogen doping levels. e) The calculated DOS of Co@NCNT and Co.

energy-saving hydrogen production and green synthesis of high value-added chemicals. Such concept of monolithic chainmail catalyst is important for achieving a highly stable and efficient catalyst for energy conversion.

## Supporting Information

Supporting Information is available from the Wiley Online Library or from the author.

## Acknowledgements

D.L. and Z.L. contributed equally to this work. This work was supported by the Science and Technology Basic Resources Investigation Program of China (Grant No. 2019FY100900), the National Key Research and Development Program of China (Grant No. 2021YFC2101604), the National Natural Science Foundation of China (Grant No. 31971614), the State Key Laboratory of Pulp and Paper Engineering (Grant No. 2022PY02), the National Program for Support of Topnotch Young Professionals (Grant No. x2qsA4210090), and the University Development Fund, Research Start-up Fund (Grant No. UDF01002976) from the Chinese University of Hong Kong (Shenzhen).

## Conflict of Interest

The authors declare no conflict of interest.

## Data Availability Statement

The data that support the findings of this study are available in the supplementary material of this article.

## Keywords

chainmail catalysts, hydrogen production, monosaccharide oxidation, tri-functional electrocatalysts, wood material

Received: February 10, 2023  
Revised: April 9, 2023  
Published online: May 10, 2023

[1] P. Zhai, Y. Zhang, Y. Wu, J. Gao, B. Zhang, S. Cao, Y. Zhang, Z. Li, L. Sun, J. Hou, *Nat. Commun.* **2020**, *11*, 5462.



- [2] X. Wu, S. Zhou, Z. Wang, J. Liu, W. Pei, P. Yang, J. Zhao, J. Qiu, *Adv. Energy Mater.* **2019**, *9*, 1901333.
- [3] Y. Li, Z. S. Wu, P. Lu, X. Wang, W. Liu, Z. Liu, J. Ma, W. Ren, Z. Jiang, X. Bao, *Adv. Sci.* **2020**, *7*, 1903089.
- [4] X. Luo, P. Ji, P. Wang, R. Cheng, D. Chen, C. Lin, J. Zhang, J. He, Z. Shi, N. Li, S. Xiao, S. Mu, *Adv. Energy Mater.* **2020**, *10*, 1903891.
- [5] H. Sun, C. Tian, G. Fan, J. Qi, Z. Liu, Z. Yan, F. Cheng, J. Chen, C. P. Li, M. Du, *Adv. Funct. Mater.* **2020**, *30*, 1910596.
- [6] W. Liu, E. Hu, H. Jiang, Y. Xiang, Z. Weng, M. Li, Q. Fan, X. Yu, E. I. Altman, H. Wang, *Nat. Commun.* **2016**, *7*, 10771.
- [7] D. C. Nguyen, D. T. Tran, T. L. L. Doan, D. H. Kim, N. H. Kim, J. H. Lee, *Adv. Energy Mater.* **2020**, *10*, 1903289.
- [8] T. V. Tam, S. G. Kang, M. H. Kim, S. G. Lee, S. H. Hur, J. S. Chung, W. M. Choi, *Adv. Energy Mater.* **2019**, *9*, 1900945.
- [9] L. He, J. Liu, Y. Liu, B. Cui, B. Hu, M. Wang, K. Tian, Y. Song, S. Wu, Z. Zhang, Z. Peng, M. Du, *Appl. Catal. B* **2019**, *248*, 366.
- [10] X. Mu, J. Gu, F. Feng, Z. Xiao, C. Chen, S. Liu, S. Mu, *Adv. Sci.* **2021**, *8*, 2002341.
- [11] Y. Pan, K. Sun, S. Liu, X. Cao, K. Wu, W. C. Cheong, Z. Chen, Y. Wang, Y. Li, Y. Liu, D. Wang, Q. Peng, C. Chen, Y. Li, *J. Am. Chem. Soc.* **2018**, *140*, 2610.
- [12] M. A. R. Anjum, J. S. Lee, *ACS Catal.* **2017**, *7*, 3030.
- [13] L. Ji, J. Wang, X. Teng, T. J. Meyer, Z. Chen, *ACS Catal.* **2019**, *10*, 412.
- [14] L. Wu, L. Yu, F. Zhang, B. McElhenny, D. Luo, A. Karim, S. Chen, Z. Ren, *Adv. Funct. Mater.* **2020**, *31*, 2006484.
- [15] Y. Zhu, G. Chen, X. Xu, G. Yang, M. Liu, Z. Shao, *ACS Catal.* **2017**, *7*, 3540.
- [16] Y. Abghoui, E. Skúlason, *J. Phys. Chem. C* **2017**, *121*, 24036.
- [17] Y. Li, R. Cao, L. Li, X. Tang, T. Chu, B. Huang, K. Yuan, Y. Chen, *Small* **2020**, *16*, 1906735.
- [18] J. Kibsgaard, Z. Chen, B. N. Reinecke, T. F. Jaramillo, *Nat. Mater.* **2012**, *11*, 963.
- [19] H. I. Karunadasa, E. Montalvo, Y. Sun, M. Majda, J. R. Long, C. J. Chang, *Science* **2012**, *335*, 698.
- [20] S. Wang, J. Wang, M. Zhu, X. Bao, B. Xiao, D. Su, H. Li, Y. Wang, *J. Am. Chem. Soc.* **2015**, *137*, 15753.
- [21] J. Jia, T. Xiong, L. Zhao, F. Wang, H. Liu, R. Hu, J. Zhou, W. Zhou, S. Chen, *ACS Nano* **2017**, *11*, 12509.
- [22] G. Humagain, K. MacDougall, J. MacInnis, J. M. Lowe, R. H. Coridan, S. MacQuarrie, M. Dasog, *Adv. Energy Mater.* **2018**, *8*, 1801461.
- [23] D. Das, K. K. Nanda, *Nano Energy* **2016**, *30*, 303.
- [24] Y.-Y. Ma, C.-X. Wu, X.-J. Feng, H.-Q. Tan, L.-K. Yan, Y. Liu, Z.-H. Kang, E.-B. Wang, Y.-G. Li, *Energy Environ. Sci.* **2017**, *10*, 788.
- [25] J. Deng, D. Deng, X. Bao, *Adv. Mater.* **2017**, *29*, 1606967.
- [26] M. Zhang, J. Guan, Y. Tu, S. Chen, Y. Wang, S. Wang, L. Yu, C. Ma, D. Deng, X. Bao, *Energy Environ. Sci.* **2020**, *13*, 119.
- [27] X. Zhang, L. Zhang, G. G. Zhu, Y. X. Zhu, S. Y. Lu, *ACS Appl. Mater. Interfaces* **2020**, *12*, 7153.
- [28] P. Duan, X. Xu, K. Guo, Q. Yue, B. Gao, *Appl. Catal. B* **2022**, *316*, 121695.
- [29] J. Deng, P. Ren, D. Deng, X. Bao, *Angew. Chem., Int. Ed.* **2015**, *54*, 2100.
- [30] W. Li, C. Wang, X. Lu, *J. Mater. Chem. A* **2021**, *9*, 3786.
- [31] H. Yang, M. Driess, P. W. Menezes, *Adv. Energy Mater.* **2021**, *11*, 2102074.
- [32] J. Yu, G. Li, H. Liu, L. Zeng, L. Zhao, J. Jia, M. Zhang, W. Zhou, H. Liu, Y. Hu, *Adv. Sci.* **2019**, *6*, 1901458.
- [33] H. Zhao, D. Lu, J. Wang, W. Tu, D. Wu, S. W. Koh, P. Gao, Z. J. Xu, S. Deng, Y. Zhou, B. You, H. Li, *Nat. Commun.* **2021**, *12*, 2008.
- [34] B. You, X. Liu, N. Jiang, Y. Sun, *J. Am. Chem. Soc.* **2016**, *138*, 13639.
- [35] Y. Li, X. Wei, L. Chen, J. Shi, M. He, *Nat. Commun.* **2019**, *10*, 5335.
- [36] K. Xiang, D. Wu, X. Deng, M. Li, S. Chen, P. Hao, X. Guo, J. L. Luo, X. Z. Fu, *Adv. Funct. Mater.* **2020**, *30*, 1909610.
- [37] G. Yang, Y. Jiao, H. Yan, Y. Xie, A. Wu, X. Dong, D. Guo, C. Tian, H. Fu, *Adv. Mater.* **2020**, *32*, 2000455.
- [38] D. W. Wakerley, M. F. Kuehnel, K. L. Orchard, K. H. Ly, T. E. Rosser, E. Reisner, *Nat. Energy* **2017**, *2*, 17021.
- [39] X. Wu, N. Luo, S. Xie, H. Zhang, Q. Zhang, F. Wang, Y. Wang, *Chem. Soc. Rev.* **2020**, *49*, 6198.
- [40] W. Li, F. Wang, Z. Zhang, S. Min, *Appl. Catal. B* **2022**, *317*, 121758.
- [41] Y. Li, T. Gao, Y. Yao, Z. Liu, Y. Kuang, C. Chen, J. Song, S. Xu, E. M. Hitz, B. Liu, R. J. Jacob, M. R. Zachariah, G. Wang, L. Hu, *Adv. Energy Mater.* **2018**, *8*, 1801289.
- [42] B. Hui, K. Zhang, Y. Xia, C. Zhou, *Electrochim. Acta* **2019**, *330*, 135274.
- [43] H. Luo, X. Zhao, T. Zhang, R. Si, X. Gong, C. Li, F. Kong, Y. Liu, J. Jiang, H. Chen, *Int. J. Hydrogen Energy* **2023**, *48*, 9244.
- [44] X. Dai, Z. Li, Y. Ma, M. Liu, K. Du, H. Su, H. Zhuo, L. Yu, H. Sun, X. Zhang, *ACS Appl. Mater. Interfaces* **2016**, *8*, 6439.
- [45] H. Jiang, J. Gu, X. Zheng, M. Liu, X. Qiu, L. Wang, W. Li, Z. Chen, X. Ji, J. Li, *Energy Environ. Sci.* **2019**, *12*, 322.
- [46] L. Yan, Y. Xu, P. Chen, S. Zhang, H. Jiang, L. Yang, Y. Wang, L. Zhang, J. Shen, X. Zhao, L. Wang, *Adv. Mater.* **2020**, *32*, 2003313.
- [47] K. Gao, B. Wang, L. Tao, B. V. Cunnings, Z. Zhang, S. Wang, R. S. Ruoff, L. Qu, *Adv. Mater.* **2018**, *31*, 1805121.
- [48] D. Zhao, K. Sun, W. C. Cheong, L. Zheng, C. Zhang, S. Liu, X. Cao, K. Wu, Y. Pan, Z. Zhuang, B. Hu, D. Wang, Q. Peng, C. Chen, Y. Li, *Angew. Chem., Int. Ed.* **2020**, *59*, 8982.
- [49] T. Liu, J. Mou, Z. Wu, C. Lv, J. Huang, M. Liu, *Adv. Funct. Mater.* **2020**, *30*, 2003407.
- [50] Z. Chen, Y. Ha, H. Jia, X. Yan, M. Chen, M. Liu, R. Wu, *Adv. Energy Mater.* **2019**, *9*, 1803918.
- [51] C. Tang, B. Wang, H. F. Wang, Q. Zhang, *Adv. Mater.* **2017**, *29*, 1703185.
- [52] Q. Qian, J. Zhang, J. Li, Y. Li, X. Jin, Y. Zhu, Y. Liu, Z. Li, A. El-Harairy, C. Xiao, G. Zhang, Y. Xie, *Angew. Chem., Int. Ed.* **2021**, *60*, 5984.
- [53] Y. X. Chen, A. Lavacchi, H. A. Miller, M. Bevilacqua, J. Filippi, M. Innocenti, A. Marchionni, W. Oberhauser, L. Wang, F. Vizza, *Nat. Commun.* **2014**, *5*, 4036.
- [54] Z. Chen, C. Liu, X. Zhao, H. Yan, J. Li, P. Lyu, Y. Du, S. Xi, K. Chi, X. Chi, H. Xu, X. Li, W. Fu, K. Leng, S. J. Pennycook, S. Wang, K. P. Loh, *Adv. Mater.* **2019**, *31*, 1804763.
- [55] Y. Zhang, H. Luo, L. Kong, X. Zhao, G. Miao, L. Zhu, S. Li, Y. Sun, *Green Chem.* **2020**, *22*, 7333.
- [56] S. Kiatphuengporn, A. Junkaew, C. Luadthong, S. Thongratkaew, C. Yimsukanan, S. Songtawee, T. Butburee, P. Khemthong, S. Namuangruk, M. Kunaseth, K. Faungnawakij, *Green Chem.* **2020**, *22*, 8572.
- [57] Y. Gao, Z. Xiao, D. Kong, R. Iqbal, Q.-H. Yang, L. Zhi, *Nano Energy* **2019**, *64*, 103879.
- [58] J. Deng, P. Ren, D. Deng, L. Yu, F. Yang, X. Bao, *Energy Environ. Sci.* **2014**, *7*, 1919.